Evaluation of global atmospheric solvers using extensions of the Jablonowski and Williamson baroclinic wave test case

Sang-Hun Park, William C. Skamarock, Joseph B. Klemp,

Laura D. Fowler and Michael G. Duda

National Center for Atmospheric Research, Boulder, CO, USA *

4 Mar. 2013

Accepted from Monthly Weather Review

Submitted on 29 Mar. 2012

First Revised on 31 Aug. 2012

Second Revised on 16 Jan. 2013

*The National Center for Atmospheric Research is sponsored by the National Science Foundation.

Corresponding author address: Sang-Hun Park, National Center for Atmospheric Research, P.O. Box 3000, Boulder, CO 80307-3000. E-mail: shpark@ucar.edu

ABSTRACT

The hydrostatic and nonhydrostatic atmospheric solvers within the Model for Prediction Across Scales (MPAS) are tested using an extension of Jablonowski and Williamson baroclinic wave test case that includes moisture. We use the dry test case to verify the correctness of the solver formulation and coding by comparing results from the two different MPAS solvers and from the global version of the Advanced Research WRF(ARW) model. A normal-mode initialization is used in Jablonowski and Williamson test, and the most unstable mode is found to be wave number 9. The three solvers produce very similar norma-mode structures and nonlinear baroclinic wave evolutions. Solutions produced using MPAS variable-resolution meshes are quite similar to the results from the quasi-uniform mesh with equivalent resolution. Importantly, the small scale flow features are better resolved in the fine-resolution region and there is no apparent wave distortion in the fine-to-coarse mesh transition region, thus demonstrating the potential value of MPAS for multiscale flow simulation.

1. Introduction

We have been developing a new modeling framework for atmospheric dynamical cores called the Model for Prediction Across Scales (MPAS; Skamarock et al. 2012, hereafter SK12). A notable feature of MPAS is the use of an unstructured horizontal mesh using Spherical Centroidal Voronoi Tessellations (SCVTs, nominally hexagons) with C-grid staggering (Thuburn et al. 2009). There are two MPAS atmospheric dynamical solvers - a hydrostatic solver (MPAS-AH) and a nonhydrostatic solver (MPAS-ANH). In this paper we compare the performance of MPAS-AH and MPAS-ANH using an extension of Jablonowski and Williamson (2006 here after JW06) case, initialized with the most unstable mode, and optionally including moisture. The normal mode initialization bypasses the initial adjustment process arising with the JW06 unbalanced initial perturbation, thus removing a source of uncertainty in evaluating the test results. Additionally, we can use the symmetry of the normal mode evolution on the sphere to examine effects of zonally anisotropic meshes. We also test global dynamical cores with simple moist physics because we have often found that the grid-scale forcing produced by moist physics provides a more stringent test of solver robustness. We specify the initial moisture such that it does not lead to a convectively unstable atmosphere, thus only a simple parameterization of the cloud microphysics is needed for this test. In order to confirm the accuracy of these solvers, we also compare these results with those from the global version of the Advanced Research WRF (ARW; Skamarock et al., 2008).

The SCVTs used in MPAS permit continuous refinement on a conformal horizontal mesh in which the coarse-to-fine mesh transitions are smooth and do not contain abrupt changes in resolution inherent in traditional grid-nesting (e.g. Warner et al. 1997). Thus, we expect that the MPAS grid refinement should reduce many problems associated with traditional grid nesting. We use the extended test cases to examine the robustness of the nonhydrostatic MPAS solver using a locally refined mesh. Recently, Ringler et al. (2011) showed good performance for the MPAS shallow-water equations solver on various locally-refined meshes, and the results from our 3D solver will further demonstrate the feasiblility of locally refined SCVTs for atmospheric applications.

Our paper is organized as follows. In section 2, the initialization algorithms for dry and moist test cases on the hydrostatic p coordinate and nonhydrostatic hybrid z coordinate are presented. The life cycle, synoptic features of the waves, intensity, and structure in quasi-uniform and variable-resolution meshes are discussed in section 3, and section 4 contains the summary remarks.

2. Model initial conditions

A detailed description of the MPAS-ANH is presented in SK12 and the model equations for the MPAS-AH are described in the Appendix. For hydrostatic-scale applications, the most significant difference between the hydrostatic and nonhydrostatic atmospheric solvers is the terrain following vertical coordinate; MPAS-AH uses a pressure-based coordinate and MPAS-ANH uses a height-based coordinate. Thus the distribution of vertical levels is necessarily different in the MPAS-AH and MPAS-ANH configurations in the following experiments.

a. MPAS-AH; Hydrostatic hybrid-sigma coordinate

To initialize the zonally homogeneous balanced state for MPAS-AH, the surface geopotential height Φ_s and temperature T are defined using Eqs. (4)-(7) in JW06 except for the inclusion of water vapor. Since we treat moisture as a part of the horizontal deviation field, we use the same formulation of the horizontal-mean temperature $< T >$ as in JW06 :

$$< T > = T_0 \left(\frac{p}{p_0}\right)^{R_d\Gamma/g} \qquad \text{for } \eta_s \geq \eta \geq \eta_t, \tag{1}$$

$$< T > = T_0 \left(\frac{p}{p_0}\right)^{R_d\Gamma/g} + \triangle T(\eta_t - \eta)^5 \qquad \text{for } \eta_t \geq \eta, \tag{2}$$

with the surface level $\eta_s = 1$, the tropopause level $\eta_t = 0.2$, the temperature at the surface $T_0 = 288K$ and $\triangle T = 4.8 \times 10^5 K$. The horizontal deviation temperature with moisture is modified to become

$$\begin{aligned}\tilde{T} &= -\frac{p}{R_d}\left(\frac{\partial \eta}{\partial p}\right)\frac{\partial \phi}{\partial \eta} \\ &= \frac{3\pi}{4}\frac{p}{R_d}\, u_0\ \sin\eta_v\ \cos^{1/2}\eta_v \\ &\times \Bigg[\left\{-2\sin^6\varphi(\cos^2\varphi + \frac{1}{3}) + \frac{10}{63}\right\} 2u_0\cos^{3/2}\eta_v \\ &\quad + \left\{\frac{8}{5}\cos^3\varphi(\sin^2\varphi + \frac{2}{3}) - \frac{\pi}{4}\right\}\Omega a\Bigg]\left(\frac{1}{p_s - p_t}\right)\left(\frac{1}{1 + 1.61 q_v}\right)\end{aligned} \tag{3}$$

where $\eta_v = (\eta - \eta_0)\frac{\pi}{2}$, $a = 6.371229 \times 10^6$ m is the mean radius of the Earth, $\Omega = 7.29212 \times 10^{-5}\ \mathrm{s}^{-1}$ is the earth's angular velocity and the other variables have their usual meaning. In our study p is defined to include moisture (in contrast to the dry atmosphere used in JW06), although dry pressure, p_d, is used for the definition of $\eta = (p_d - p_t)/(p_0 - p_t)$ (whereas $\eta = p/p_0$ in JW06). This vertical coordinate definition is equivalent to the more general hybrid coordinate from in (A1) since $p_0 = p_s$ for this test case. The relationship between dry and moist pressure is

$$\frac{\partial p}{\partial \eta} = (1 + q_v)\frac{\partial p_d}{\partial \eta}, \tag{4}$$

and the specific volume for dry air, α_d, is calculated from ideal gas law as

$$\alpha_d = \frac{R_d}{p_0}\theta(1 + 1.61 q_v)\left(\frac{p}{p_0}\right)^{-c_v/c_p}. \tag{5}$$

The moisture is specified in terms of the relative humidity,

$$RH = \begin{cases} 0 & \text{for } p < 500\text{hPa}, \\ \min\left[0.4, \left(1 - \frac{p_0 - p}{500\text{hPa}}\right)^{1.25}\right] & \text{for } p \geq 500\text{hPa}. \end{cases} \tag{6}$$

and geopotential height is calculated from the hydrostatic equation (A10) as

$$\frac{\partial \phi}{\partial \eta} = -\alpha_d \frac{\partial p_d}{\partial \eta}. \tag{7}$$

The equations (1)-(7) are solved iteratively to satisfy the hydrostatic condition in each column.

In order to calculate the geostrophically balanced condition including moisture, we iteratively solve the nonlinear equation for zonal wind u_e using the analytic form of geostrophic wind on the Voronoi mesh:

$$-2fu_e^{n+1}\sin\psi = \frac{(u_e^n)^2}{a}\tan\varphi\ \sin\psi - PGF_{SCVTs}, \tag{8}$$

where n is the iteration number, $f = 2\Omega\sin\varphi$ is Coriolis force, ψ is the angle between the edge and north pole, PGF_{SCVTs} is the pressure gradient formulation in (A16) and u_e is the zonal velocity ($u_e = u\cos\psi + u_T\sin\psi$, where u is the normal and u_T is the tangential vector at the edge). Equation (8) is solved using the converged solution of (1)-(7) to compute the PGF term. We begin the iterations using the JW06 zonal wind (their Eq. (2)) and convergence is reached when $|u_e^{n+1} - u_e^n| < 10^{-5}$. Figure 1 shows the atmospheric structure for the hydrostatic initialization for the dry (Fig. 1(a)) and moist (Fig. 1(b)) cases. Although the maximum zonal winds in these two cases differ slightly, the overall structures are quite similar.

b. MPAS-ANH; Nonhydrostatic hybrid height coordinate

The height-based vertical coordinate of the MPAS-ANH follows Klemp (2011) and has the form

$$z = \zeta + A(\zeta)z_s(\vec{\mathbf{x}}_H, \zeta). \tag{9}$$

ζ represents the nominal heights (without terrain) of the coordinate surfaces, $A(\zeta)$ defines the relative weighting between the terrain-following coordinate and the pure height coordinate with $0 \le A \le 1 - \zeta/z_T$, and the array z_s is a progressively smoothed representation of terrain with requirement that $z_s(\vec{\mathbf{x}}_H, 0)$ is the actual terrain ($\vec{\mathbf{x}}_H$ denoting the horizontal coordinate). For the testing described here, the basic terrain following form is used, in which $A = 1 - \zeta/z_T$ and $z_s(\vec{\mathbf{x}}_H, \zeta) = z_s(\vec{\mathbf{x}}_H, 0)$.

In initializing the nonhydrostatic model, we define reference and perturbation values for the thermodynamic variables. As in the hydrostatic case, an iterative procedure is employed to obtain the perturbation values. The dry reference state value is defined based on an isothermal atmosphere:

$$\overline{p} = p_0 e^{-gz/R_d T_0}, \tag{10}$$

$$\overline{\pi} = \left(\frac{\overline{p}}{p_0}\right)^{R_d/c_p}, \tag{11}$$

$$\overline{\rho} = \frac{\overline{p}}{R_d T_0}, \tag{12}$$

$$\overline{\theta} = T_o/\overline{\pi}, \tag{13}$$

and

$$\overline{\Theta} = \overline{\rho}\overline{\theta} \tag{14}$$

where $T_0 = 250K$, other variables have their usual meaning and the overline refers to the reference state which is function of z only. For the temperature profile, we first obtain the temperature deviation, $\tilde{T}$, from the global horizontal-average temperature, $< T >$, and thus derive the total temperature with a formulation similar to (1) - (3). The temperature deviation from the globally averaged temperature is defined including moisture:

$$\tilde{T} = -\frac{p}{R_d}\frac{1}{(1+0.61q_v)}\left(\frac{\partial \eta}{\partial p}\right)\frac{\partial \phi}{\partial \eta}, \tag{15}$$

where $\tilde{T} = T - < T >$. Water vapor, q_v, is calculated from the relative humidity (6). We define a temperature T_m as

$$T_m = (< T > + \tilde{T})(1 + 1.61q_v). \tag{16}$$

The density perturbation, ρ', is derived using the actual temperature perturbation value, $T_m - T_0$, as

$$\rho' = \left[\frac{p'}{R_d} - \overline{\rho}(T_m - T_0)\right] / T_m \tag{17}$$

and perturbation pressure p' is recovered from the hydrostatic equation

$$\frac{\partial p'}{\partial z} = -g(\rho' + \rho q_v). \tag{18}$$

Equations (15) - (18) are iterated to produce the hydrostatically balanced thermodynamic variables. As in the hydrostatic model initialization, we recompute the geostrophic wind using (8). Fig. 2 shows the initial profile from MPAS-ANH. The result using (8) is comparable with the different approach in SK12 which used the 2-D zonally uniform mesh to interpolate it to the 3-D mesh (see Figure 6 in SK12). Both the dry (Fig. 2(a)) and moist (Fig. 2(b)) states are very similar to those from the hydrostatic model (Fig. 1). As JW06 suggested, a simulation without any perturbation is a stringent test to investigate the ability of model to maintain an initially balanced jet. Test results from this initialization for MPAS-ANH are shown in SK12 (see their Figure 9) for the dry case.

3. Results

a. Quasi-uniform mesh

The test case is an extension of the well-known JW06 case that employs an isolated perturbation producing short baroclinic wave train (simulated with MPAS-ANH in SK12). In this paper, we focus on the life cycle of the most unstable normal mode. Similar simulations have been performed in many other studies, for example Simmons and Hoskins (1978, hereafter SH78) on the sphere, and Snyder et al. (1991), Rotunno et al. (1994), Whitaker and Davis (1994, hereafter WD94), Zhang (2004), Plougonven and Snyder (2007) and Waite and Snyder (2009) in a periodic channel.

To isolate each normal mode, we introduce a u field perturbation for the appropriate zonal wave number onto the balanced JW06 jet initialization described in the Section 2. The normal modes for MPAS-AH and MPAS-ANH are calculated iteratively by repeatedly integrating forward three days and then renormalizing the perturbations to a reference amplitude, in this case the maximum in the lowest level meridional wind (we use the reference amplitude $v_{max} = 1.20$ m/s in all our tests). Through this process, we find that wave number 9 is the most unstable mode for the two models, and thus we will use this mode in our test case simulations. This most unstable normal mode does not appear to be biased by grid imprinting since as discussed in SK12 and Lauritzen et al. (2010), on global icosahedral meshes tend to excite disturbances at wave number 5 or 10. Wave number 9 is further confirmed by equivalent simulations with the WRF-ARW, which employs a lat-lon horizontal grid.

The model configurations for the simulated cases are summarized in Table 1. The control mesh has 40962 cells having mean cell center spacing of about 120 km. MPAS uses the same Runge-Kutta time integration scheme (Wicker and Skamarock (2002)) as used in ARW, and it uses the 3rd-order transport scheme and monotonic limiter described in Skamarock and Gassmann (2011, hereafter SG11). We use the kinetic energy formulation from SK12 equation (14) with the coefficient $\alpha = 3/8$. Second order horizontal diffusion is used with coefficients $K_2 = 10^5$ and $10^4\ \mathrm{m^2 s^{-1}}$ for the linear and nonlinear simulations, respectively, for reasons that will be discussed later in this section. We have performed tests using a 4^{th}-order hyper-diffusion and we have not found any significant differences in the results compared to experiments using second-order diffusion. In addition, the non-hydrostatic model uses 3D divergence damping with the coefficient of $\beta_d = 0.1$ and a vertically implicit off-centering parameter ($\beta_s = 0.1$) [See Klemp et al. (2007)]. In this paper, all parameterized physics are excluded except for the Kessler microphysics scheme (Kessler, 1969) as implemented by Klemp and Wilhelmson (1978).

1) Linear mode

In this section, the converged normal mode solutions for wave number 9 are analyzed. The surface pressure perturbations are shown in Fig. 3 for the dry and moist experiments. Since the simulations are zonally periodic, only a portion of the wave train is plotted. The size, shape, and intensity of the gradients between the cyclone and anti-cyclone are quite similar in both the hydrostatic and nonhydrostatic models. SH78 and Balasubramanian and Garner (1997, hereafter BG97) showed that the tilt of normal mode depends on the jet structure (background shear) and wavelength. The contours in Fig. 3 are similar with a biased NE-SW (anticyclonic) tilt in the southern part of wave that is caused by horizontal eddy momentum fluxes (BG97). Because of strong poleward eddy momentum fluxes at the surface (not shown), the location of pressure (Fig. 3) perturbations are also displaced a few degrees poleward of the maximum jet region. Like the surface pressure perturbation, all other variables such as velocity and geopotential height compare similarly in the MPAS-AH and MPAS-ANH simulations (not shown).

In the literature, regardless of grid type [Cartesian grid (Joly and Thorpe, 1989 and WD94) and spherical mesh (Govindasamy and Garner (1997), hereafter GG97)], the growth rates of the most unstable modes in moist simulations are larger than in the dry case. Figure 4 shows the time series of the maximum meridional velocity at the lowest level during the 6-day integration beginning from the normal mode solutions. In this study, as shown in Fig. 4, we obtain similar growth rates between dry and moist cases because we use smaller amounts of moisture to avoid convective instability, and thus there is no condensation during linear growth rate to the converged normal-mode solution.

2) Nonlinear mode evolution

Midlatitude baroclinic waves develop as the perturbations grow from the linear normal mode structure. These experiments are initiated with the same normal mode amplitude and have nearly identical structures. The moist effects are small at early times (condensation doesn't occur until day 3.5). Due to the nonlinear condensational heating after day 4, the increase of maximum velocity in the moist cyclone is slightly faster than in the dry case. After day 5.5, the baroclinic waves reach their breaking stage and the meridional wind speeds begin to decrease. The dry MPAS-AH case shows a little bit slower onset of the cyclonic breaking stage compared to the other simulations in Fig. 4.

A comparison of the hydrostatic and nonhydrostatic solutions for the dry case from day 3 to day 5 is shown in Fig. 5, and the minimum and maximum surface pressures during the integration are summarized in Table. 2. At day 3, both MPAS-AH and MPAS-ANH have similar intensities and asymmetric patterns for the low and high pressure areas. The increasing asymmetries in the cyclonic surface pressures are clearly evident; by day 4 the magnitude of the lowest pressure perturbations are twice as large as the highest pressures and continuously amplifying in both simulations. The poleward (equatorward) displacements of the cyclones (anticyclones) can be seen in both the hydrostatic and nonhydrostatic cases on day 4 and 5. In order to further verify the correctness of the solver formulations and coding, we carried out the same simulations using global ARW with the same distribution of vertical levels as JW06 and MPAS-AH. The results are plotted in Fig. 6 and they show that there are no visible differences between hydrostatic and nonhydrostatic ARW simulations. We can also see that both the hydrostatic and nonhydrostatic ARW results are very similar to the MPAS-AH shown in Fig. 5. As seen from the MPAS-ANH result with $K_2 = 10^4$ in Table 2 and the results with hyper diffusion and two-dimensional deformation-dependent mixing coefficients in the ARW and MPAS-ANH in Table 3, the intensity of the waves with different diffusion schemes are very comparable. Thus, unlike the initial perturbation test such as Polvani et al. (2004), there is no significant sensitivity to different diffusion schemes. Both MPAS and ARW display the biased NE-SW tilted pattern as shown in the linear mode. The anticyclone is much more tilted than the cyclone, thus the synoptic wave exhibits an almost northerly flow in the cold air west of surface low and southwesterly flow in the warm air east of low. GG97 stressed that, if the initial jet structure is comparatively wide, all normal modes will have biased NE-SW tilted patterns regardless of wave number. The shape of the jet structure in our case has weak horizontal shear and a much wider shape compared to GG97 [see Figure 1(a) in GG97], however the dynamics of the jet evolution are consistent with SH78 and GG97. The moist case results for MPAS, shown in Fig. 7, also possess quite similar horizontal structure and intensity for the surface pressure and temperature, and also have the well-known synoptic baroclinic wave structure with the warm core "seclusion" and bent-back warm front as depicted in Fig. 5.

b. Moist test case with variable-resolution mesh

Using the unstructured horizontal mesh based on SCVTs, we have performed simulations of the moist test case with variable resolution. Only MPAS-ANH results will be shown here, but MPAS-AH also produces very similar results.

As Ringler et al. (2008) has shown, SCVTs allow for flexible, smoothly changing mesh size while maintaining the conformal property. Detailed reviews of SCVT generation techniques are given by Ju et al. (2010) and Ringer et al. (2008). The variable-resolution mesh we use has 40962 cells, with cell-center spacings $\triangle_{cell} \sim 53$ km for the finest mesh region and $\triangle_{cell} \sim 210$ km for the coarsest mesh region. Regarding solver efficiency for this variable mesh, we are using a single fixed time step for the global domain, which is constrained by the finest mesh spacing. Although the computational efficiency could be improved by using different time steps for coarse and fine portions of the domain, since most of the cells may be located in the fine-mesh region, the efficiency gains from using different time steps in different regions of the mesh may be small.

A coarser version of the variable-resolution mesh (5762 cells) is shown in Fig. 8(a) to show the global structure. The uniform fine mesh area is centered at (0°E, 50°N), which is our target area, and through the transitional zone the mesh relaxes smoothly to a uniform coarser mesh outside the target area. A more detailed view of the mesh structures in the transitional zone is shown in Fig. 8(b). We will refer each box shown in Fig. 8(b) as LEFT (90°W $\sim$ 30°W), CENTER (30°W $\sim$ 30°E) and RIGHT (30°E $\sim$ 90°E) with the same latitude (20°N $\sim$ 80°N). The development (day 4) and occlusion (day 5) of the baroclinic wave on the variable-resolution mesh are shown in Fig. 9. This simulation is carried out using a constant diffusion coefficient as indicated in Table 1, and the waves have the same structure and the same large scale features as obtained with the quasi uniform mesh in Fig. 7 at day 4 and at day 5 : On day 4, condensation begins east of the low, and an asymmetric pattern develops between the east and west sides of the cyclone with large gradients in surface pressure in the cyclonic area and a NE-SW tilt of the anticyclone. Minimum/maximum surface pressures for LEFT, CENTER and RIGHT regions are summarized in Table 4, and are quite similar to the quasi-uniform mesh results in Table 2. As the baroclinic waves passes through the high-resolution area, there are no noticeable wave distortions or reflections. Fig. 10 shows the vertically integrated rain water at day 5.5. There are noticeable differences in rain intensity between the regions of differing resolution. Compared to the quasi-uniform mesh results depicted in Fig 10(a) and the coarse-resolution region in the variable-resolution mesh in Fig. 10(b), the rain pattern from the high-resolution region shows a stronger intensity because the condensation and vertical cloud water flux, driven by fine-scale flow convergence, is stronger in the high-resolution region.

4. Summary

To evaluate the initial performance and robustness of the new global dynamical cores MPAS-AH and MPAS-ANH, we have produced simulations using modification of the JW06 baroclinically unstable jet initialized with a single (most unstable) normal mode with and without moisture. We use these simulations to examine the structures of the most unstable normal mode and its nonlinear evolution, and document that the MPAS and global ARW models produce equivalent results. The simulations are carried out for dry and moist cases with quasi-uniform and variable-resolution meshes.

Since the flow is baroclinically unstable, any imbalance will grow and produce amplifying waves. We find the most unstable mode is wave number 9 in both MPAS-AH and MPAS-ANH solutions. Importantly, we do not see grid imprinting from the wave numbers 5 and 10 that could arise on the icosahedral mesh configuration. From simulations with different diffusion schemes in MPAS and the global ARW, we find that there is no significant dependency on the diffusion scheme in this test case.

For both the hydrostatic and nonhydrostatic simulations initialized with the normal mode, full lifecycles of baroclinic waves evolve from the growing to decaying phases of their nonlinear evolution. The structures and intensities in the dry and moist cases are similar because we use only a small amount of moisture in the initial state. Only a small amount of water vapor is used in this test because it produces condensation without convective instability and thus requires only a simple microphysics scheme in the model. The diabatic heating provides significant small-scale forcing that can stress the models, and we find that both hydrostatic and nonhydrostatic models are robust even with this diabatic heating. As expected, since the mesh size is still too large to simulate nonhydrostatic effects, there is little difference between the hydrostatic and nonhydrostatic results.

One of the main potential benefits of MPAS is the flexibility in specifying variable resolution, allowed by the horizontal spherical centroidal voronoi meshes. For this test case, MPAS produces consistent and similar results in all regions of the variable-resolution mesh, i.e. in the fine-mesh region, in the transitional region and in the coarse-mesh region. There are no noticeable reflections or distortions in the mesh-transition regions, and each of the nine waves have similar structures. Small-scale structures are better simulated in the fine-mesh region and we still observe the basic structures of the mid-latitude baroclinic wave in the coarse-mesh region. These positive results provide evidence for the applicability of MPAS in global forecasting or climate applications with variable-resolution meshes. The results also illustrate the value of using a normal mode initialization because the zonal symmetry allows us to easily observe possible grid-imprinting and coding errors, and the influence of variable resolution. This zonal symmetry case should also be helpful in identifying scale-aware physics issues, which are significant both for uniform-resolution simulations with different grid spacings and for variable-resolution simulations. The role of model filters on variable-resolution meshes also needs to be further investigated. In this paper we used a constant filter coefficient regardless of mesh size, but further research should be directed toward determining how filtering should be designed for variable-resolution meshes.

APPENDIX

Moist hydrostatic equations for MPAS-AH

For the vertical coordinate, we employ a hybrid sigma-pressure coordinate similar to the NCAR Community Atmospheric Model (CAM):

$$p_d = B(\eta)(p_s - p_t) + [\eta - B(\eta)](p_0 - p_t) + p_t, \tag{A1}$$

where p_d is the hydrostatic pressure of dry air, p_0 is a reference sea-level pressure and p_s, p_t are the hydrostatic surface pressure and the top level pressure for dry air, respectively. (This coordinate representation differs from CAM in that it is based on dry pressure instead of full pressure and is normalized using p_t such that $\eta = 0$ at $p_d = p_t$.) Here, $B(\eta)$ defines the relative weighting of the terrain following coordinate versus the normalized pressure coordinate, such that $0 \leq B(\eta) \leq \eta$, with the limits:

$$\eta = \frac{p_d - p_t}{p_s - p_t} \qquad \text{for } B(\eta) = \eta, \tag{A2}$$

$$\eta = \frac{p_d - p_t}{p_0 - p_t} \qquad \text{for } B(\eta) = 0. \tag{A3}$$

To provide mass and scalar conservation we define the flux variables

$$(\mathbf{V}_H, \Omega, \Theta, Q_j) = \mu_d \cdot (\mathbf{v}_H,\, \dot{\eta},\, \theta,\, q_j), \tag{A4}$$

where q_j represents the mixing ratio of the respective water species and

$$\mu_d(x, y, z, t) = \frac{\partial p_d}{\partial \eta} = \frac{\partial B(\eta)}{\partial \eta}(p_s - p_t) + \left(1 - \frac{\partial B(\eta)}{\partial \eta}\right)(p_0 - p_t). \tag{A5}$$

Note this is generalized from ARW where $\mu_d(x,y,t) = p_s - p_t$. The inviscid prognostic hydrostatic equations are then expressed as :

$$\frac{\partial \mathbf{V}_H}{\partial t} + \mu_d(\alpha_m \nabla_\eta p + \nabla_\eta \phi) = -(\nabla \cdot \mathbf{V}\mathbf{v}_H)_\eta - f\mathbf{k} \times \mathbf{V}_H = F_{V_H} \quad \text{(A6)}$$

$$\frac{\partial \mu_d}{\partial t} + (\nabla \cdot \mathbf{V})_\eta = 0 \quad \text{(A7)}$$

$$\frac{\partial \Theta}{\partial t} = -(\nabla \cdot \mathbf{V}\theta)_\eta + F_\Theta = R_\Theta \quad \text{(A8)}$$

$$\frac{\partial Q_j}{\partial t} = -(\nabla \cdot \mathbf{V} q_j)_\eta + F_{Q_j} \quad \text{(A9)}$$

together with diagnostic relations for dry hydrostatic equation

$$\frac{\partial \phi}{\partial \eta} = -\alpha_d \mu_d, \quad \text{(A10)}$$

the moist hydrostatic equation

$$\frac{\partial p}{\partial \eta} = \mu_d(1 + q_v + q_c \cdots), \quad \text{(A11)}$$

and the gas law

$$p = p_0 \left(\frac{R_d \theta_m}{p_0 \alpha_d} \right)^{c_p/c_v}. \quad \text{(A12)}$$

Here $\mathbf{V} = (\mathbf{V}_H, \Omega), \theta_m = \theta[1 + (R_v/R_d)q_v], \alpha_m$ is the specific volume of moist air, f is Coriolis force and ϕ is geopotential height. Integrating (A7) vertically from the surface to the material surface at the top of the domain yields

$$\int_1^0 \frac{\partial \mu_d}{\partial t}\, d\eta = \frac{\partial}{\partial t} \int_1^0 \left(\frac{\partial p_d}{\partial \eta} \right) d\eta = -\frac{\partial p_s}{\partial t} = \int_0^1 \nabla \cdot \mathbf{V}_H \, d\eta, \quad \text{(A13)}$$

which allows p_s to be stepped forward in time. μ_d can then be computed directly from the specification of the vertical coordinate in (A5), and Ω is obtained from the stepwise vertical integration of (A7):

$$\Omega = -\int_1^\eta \frac{\partial}{\partial t} \left(\frac{\partial p_d}{\partial \eta} \right) + \nabla \cdot \mathbf{V}_H \, d\eta = -\int_1^\eta \left(B_\eta \frac{\partial p_s}{\partial t} + \nabla \cdot \mathbf{V}_H \right) d\eta. \quad \text{(A14)}$$

In order to achieve desired conservation properties on an unstructured C-grid, we write the horizontal momentum equations in vector invariant form similar to SK12:

$$\frac{\partial \mathbf{V}_H}{\partial t} + \mu_d(\alpha_m \nabla_\eta p + \nabla_\eta \phi) = -(\zeta + f)\mathbf{k} \times \mathbf{V}_H - \mathbf{v}_H \nabla_\eta \cdot \mathbf{V} - \mu_d \nabla_\eta K - \frac{\partial}{\partial \eta}(\Omega \mathbf{v}_H) = F_{V_H} \quad \text{(A15)}$$

where ζ is the relative vertical vorticity and $K = |\mathbf{v}_H|^2/2$ is the horizontal kinetic energy.

The hydrostatic equation set (A6)-(A9) is integrated forward in time using a time-splitting approach that explicitly integrates terms responsible for the fast modes (Lamb wave, gravity waves) on a smaller time step ($\triangle\tau$) while updating the slow-mode terms (advection, physics, Coriolis and diffusion) over a large time interval ($\triangle t$). The large time step is integrated using third-order Runge-Kutta scheme [Wicker and Skamarock (2002)] and a forward-backward method is used for small time step as in WRF [Skamarock et al. (2008)] and MPAS-ANH [Skamarock et al. (2012)]. Thus, the equations are stepped forward using forward-backward differencing in the following order on the small time steps while holding the slow-mode terms and coefficients fixed during each Runge-Kutta's substep (t^*) :

$$\mathbf{V}_H^{\tau+\triangle\tau} = \mathbf{V}_H^{\tau} - \triangle\tau\mu_d^{\tau}(\alpha_m^{\tau}\nabla_\eta p^{\tau} + \nabla_\eta\phi^{\tau}) + \triangle\tau F_{V_H}^{t^*} \tag{A16}$$

$$p_s^{\tau+\triangle\tau} = p_s^{\tau} + \triangle\tau\int_1^0 \nabla\cdot\mathbf{V}_H^{\tau+\triangle\tau}\,d\eta \tag{A17}$$

$$\mu_d^{\tau+\triangle\tau} = B_\eta(p_s^{\tau+\triangle\tau} - p_t) + (1-B_\eta)(p_0 - p_t) \tag{A18}$$

$$\Omega^{\tau+\triangle\tau} = -\int_1^\eta \left(B_\eta\frac{\partial p_s}{\partial\tau} + \nabla\cdot\mathbf{V}_H^{\tau+\triangle\tau}\right) d\eta \tag{A19}$$

$$\Theta^{\tau+\triangle\tau} = \Theta^{\tau} - \triangle\tau[\nabla\cdot(\mathbf{V}^{\tau+\triangle\tau} - \mathbf{V}^{t})\theta^{t}]_\eta + \triangle\tau R_\Theta^{t^*} \tag{A20}$$

$$\frac{\partial p}{\partial\eta}^{\tau+\triangle\tau} = \mu_d^{\tau+\triangle\tau}(1+q_v+q_c+\cdots)^{t^*} \tag{A21}$$

$$\alpha_d^{\tau+\triangle\tau} = \frac{R_d}{p_0}\left(1+\frac{R_d}{R_v}q_v^t\right)\left(\frac{p^{\tau+\triangle\tau}}{p_0}\right)^{-c_p/c_v}\theta^{\tau+\triangle\tau} \tag{A22}$$

$$\frac{\partial\phi}{\partial\eta}^{\tau+\triangle\tau} = -\alpha_d^{\tau+\triangle\tau}\mu_d^{\tau+\triangle\tau} \tag{A23}$$

Here, the hydrostatic equation (A21) is integrated downward from the top of the domain where $p = p_t$, and the dry hydrostatic equation (A23) is integrated upward from the surface where $\phi = gz_s(x,y)$ with surface height z_s. Notice that in (A20), the flux divergence term for the small time steps is expressed as the difference from its value at time t. This allows the full flux divergence in R_Θ^t to be evaluated with higher order numerics without impacting the small time step computations (see Klemp et al. (2007)).

REFERENCES

Balasubramanian, G. and S. T. Garner, 1997: The role of eddy momentum fluxes in shaping the life cycle of a baroclinic wave. *J. Atmos. Sci.*, **54**, 510–533.

Govindasamy, B. and S. T. Garner, 1997: The equilibration of short baroclinic waves. *J. Atmos. Sci.*, **54**, 2850–2871.

Jablonowski, C. and D. L. Williamson, 2006: A baroclinic instability test case for atmospheric model dynamical cores. *Qaurt. J. Roy. Meteor. Soc.*, **132**, 2943–2975.

Joly, A. and J. Thorpe, 1989: Warm and occluded fronts in two-dimensional moist baroclinic instability. *Qaurt. J. Roy. Meteor. Soc.*, **115**, 513–534.

Ju, L., T. D. Ringler, and M. Gunzburger, 2010: Voronoi tessellations and their application to climate and global modeling. *Numerical Techniques for Global Atmospheric Models*, P. H. Lauritzen, C. Jablonowski, M. A. Taylor, and R. D. Nair, Eds., Springer, 1–30.

Kessler, E., 1969: On the distribution and continuity of water substance in atmospheric circulations. No. 32 Amer. Meteor. Soc., 84 pp.

Klemp, J. B., 2011: A terrain following coordinate with smoothed coordinate surfaces. *Mon. Wea. Rev.*, **139**, 2163–2169.

Klemp, J. B., W. C. Skamarock, and J. Dudhia, 2007: Conservative split-explicit time integration methods for the compressible nonhydrostatic equations. *Mon. Wea. Rev.*, **135**, 2897–2913.

Klemp, J. B. and R. B. Wilhelmson, 1978: The simulation of three-dimensional convective storm dynamics. *J. Atmos. Sci*, **35**, 1070–1096.

Lauritzen, P. H., C. Jablonowski, M. A. Taylor, and R. D. Nair, 2010: Rotated versions of the Jablonowski steady-state and baroclinic wave test cases: A dynamical core intercomparison. *J. Adv. Model. Earth Sys.*, **2**, 1–41.

Plougonven, R. and C. Snyder, 2007: Inertiagravity waves spontaneously generated by jets and fronts. part i: Different baroclinic life cycles. *J. Atmos. Sci.*, **64**, 2502–2520.

Polvani, L. M., R. K. Scott, and S. J. Thomas, 2004: Numerically converged solutions of the global primitive equations for testing the dynamical core of atmospheric GCMs. *Mon. Wea. Rev.*, **132**, 2539–2552.

Ringer, T. D., L. Ju, and M. Gunzburger, 2008: A multiresolution method for climate system modeling: application of spherical centroidal Voronoi tessellations. *Ocean Dynamics*, **58**, 475–498.

Ringler, T. D., D. Jacobsen, M. Gunzburger, L. Ju, M. Duda, and W. Skamarock, 2011: Exploring a multi-resolution modeling approach within the shallow-water equations. *Mon. Wea. Rev.*, **139**, 3348–3368.

Rotunno, R. C., C. Snyder, and W. C. Skamarock, 1994: An analysis of frontogenesis in numerical simulations of baroclinic waves. *J. Atmos. Sci.*, **51**, 3373–3398.

Simmons, A. J. and B. J. Hoskins, 1978: The life cycles of some nonlinear baroclinic waves. *J. Atmos. Sci.*, **35**, 414–432.

Skamarock, W. C. and A. Gassmann, 2011: Conservative transport schemes for spherical geodesic grids: High-order flux operators for ODE-based time integration. *Mon. Wea. Rev.*, **139**, 2962–2975.

Skamarock, W. C., J. B. Klemp, L. D. Fowler, M. G. Duda, S.-H. Park, and T. D. Ringler, 2012: A multi scale nonhydrostatic atmospheric model using centroidal Voronoi tesselations and C-grid staggering. *Mon. Wea. Rev.*, **140**, 3090–3105.

Skamarock, W. C., et al., 2008: A description of the advanced research wrf version 3. NCAR Tech. Note NCAR/TN-475+STR, 113 pp.

Snyder, C., W. C. Skamarock, and R. Rotunno, 1991: A comparison of primitive-equation and semigeostrophic simulations of baroclinic waves. *Mon. Wea. Rev.*, **48**, 2179–2194.

Thuburn, J., T. Ringler, W. Skamarock, and J. Klemp, 2009: Numerical representation of geostrophic modes on arbitrarily structured C-grids. *J. Comp. Phys.*, **228**, 8321–8335.

Waite, M. L. and C. Snyder, 2009: The mesoscale kinetic energy spectrum of a baroclinic life cycle. *J. Atmos. Sci.*, **66**, 883–901.

Warner, T. T., R. A. Peterson, and R. E. Treadon, 1997: A tutorial on lateral boundary conditions as a basic and potentially serious limitation to regional numerical weather prediction. *Bull. Amer. Meteor. Soc.*, **78**, 2599–2617.

Whitaker, J. S. and C. A. Davis, 1994: Cyclogenesis in a saturated environment. *Mon. Wea. Rev.*, **51**, 889–907.

Wicker, L. J. and W. C. Skamarock, 2002: Time-splitting methods for elastic models using forward time schemes. *Mon. Wea. Rev.*, **130**, 2088–2097.

Zhang, F., 2004: Generation of mesoscale gravity waves in upper- tropospheric jetfront systems. *J. Atmos. Sci.*, **61**, 440–457.

List of Tables

TABLE 1. Configuration for the normal mode simulations.

	quasi-uniform mesh	variable-resolution mesh
total number of cell	40962	40962
$\triangle_{cell}$	$\triangle_{cell}^{\text{avg.}} \sim 120$ km	$\triangle_{cell}^{\text{min.}} \sim 53$ km, $\triangle_{cell}^{\text{max.}} \sim 210$ km
time integration	3^{rd} Runge-Kutta	3^{rd} Runge-Kutta
$\triangle t$	900 s	450 s
vertical level	26	26
transport scheme	3^{rd}-order (SG11)	3^{rd}-order (SG11)
microphysics	Kessler (1969) scheme	Kessler (1969) scheme
diffusion coefficient (K_2)	10^5 (linear) 10^4 (nonlinear)	10^5 (linear) 10^4 (nonlinear)
kinetic energy mixing (α)	0.375	0.375
divergence damping (β_d)	0.1	0.1
vertically implicit off-centering (β_s) (only for MPAS-ANH)	0.1	0.1
external-mode filtering (β_e) (only for MPAS-AH)	0.01	none

TABLE 2. Minimum and maximum surface pressure (hPa) for the quasi-uniform mesh-simulation during the nonlinear evolution, using 2^{nd}-order diffusion ($K_2 = 10^4$).

	DRY		MOIST	
Day	MPAS-AH	MPAS-ANH	MPAS-AH	MPAS-ANH
3	991.6/1006.5	991.6/1006.9	990.8/1006.9	990.8/1006.3
3.5	987.3/1008.6	986.1/1008.3	985.7/1009.2	984.8/1009.0
4	979.2/1011.1	977.7/1012.5	977.7/1011.9	975.6/1013.0
4.5	971.1/1014.0	967.1/1014.1	966.7/1014.9	964.1/1015.3
5	959.5/1016.8	958.7/1017.2	955.9/1017.9	955.3/1018.6
5.5	955.4/1019.8	955.5/1022.4	951.7/1020.8	953.1/1021.8
6	953.7/1022.6	954.6/1023.4	951.1/1023.5	952.6/1024.8

TABLE 3. Same as Table 3 except for different diffusion schemes and using global ARW.

Day	DRY			
	MPAS-ANH ($K_4 = 10^{12}$)	MPAS-ANH (2D. Smagorinsky)	WRF ($K_2 = 10^4$)	WRF (2D. Smagorinsky)
3	989.9/1007.0	990.1/1006.9	991.0/1006.6	990.8/1006.6
3.5	984.0/1009.5	984.3/1009.4	986.1/1008.9	985.8/1008.9
4	974.9/1012.4	975.9/1012.2	978.3/1011.5	978.0/1011.6
4.5	971.1/1015.4	965.7/1015.2	968.6/1014.4	968.3/1014.4
5	956.0/1018.6	958.1/1018.3	959.7/1017.3	960.0/1017.3
5.5	953.5/1021.9	955.1/1021.3	955.4/1020.2	956.1/1020.2
6	952.6/1025.0	954.1/1024.0	953.8/1023.2	954.8/1023.0

Table 4. Minimum and maximum surface pressure (hPa) for the variable-resolution mesh-simulation during the nonlinear evolution.

Day	LEFT	CENTER	RIGHT
3	990.6/1006.9	990.7/1006.9	990.6/1006.9
3.5	985.0/1009.5	985.1/1009.5	985.1/1009.4
4	976.1/1012.5	975.7/1012.5	975.8/1012.3
4.5	964.0/1015.8	962.8/1015.7	963.7/1015.5
5	954.4/1019.2	954.5/1019.2	955.3/1018.9
5.5	951.6/1022.4	951.5/1022.3	952.6/1022.3
6	951.2/1026.1	948.3/1025.2	951.1/1025.6

List of Figures

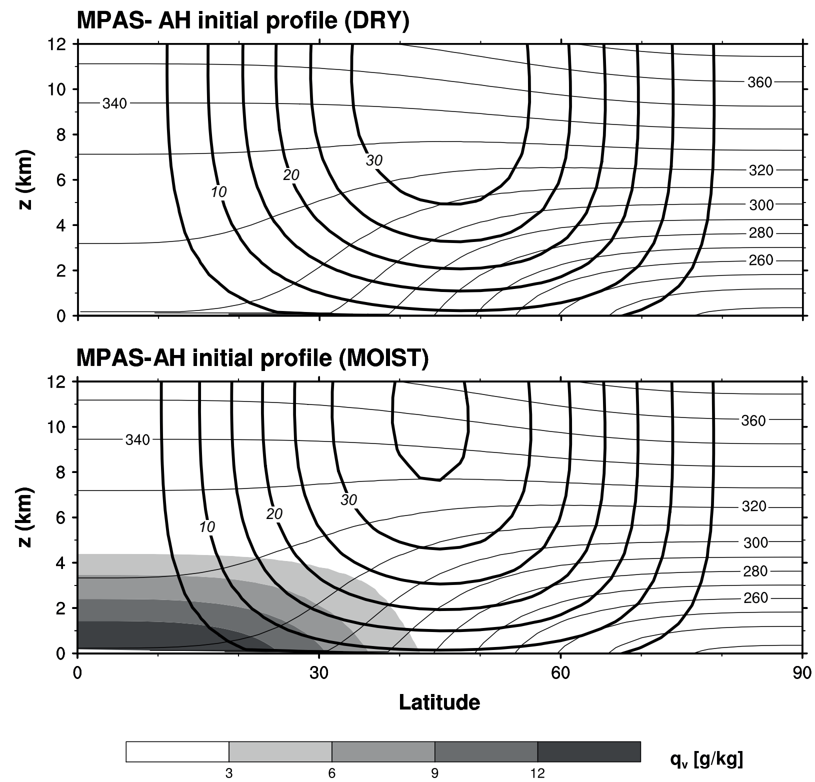

FIG. 1. The dry (top, $u_{max} = 35$ m/s) and moist (bottom, $u_{max} = 35.98$ m/s and $q_{v\,\max} = 15.21$ g/kg) jets from the MPAS hydrostatic initialization. Plotted are the zonal winds (solid thick line), θ (solid thin line) and water vapor mixing ratio (q_v, color shading). Contour line interval is 5 m/s, 10K for zonal wind and θ, respectively.

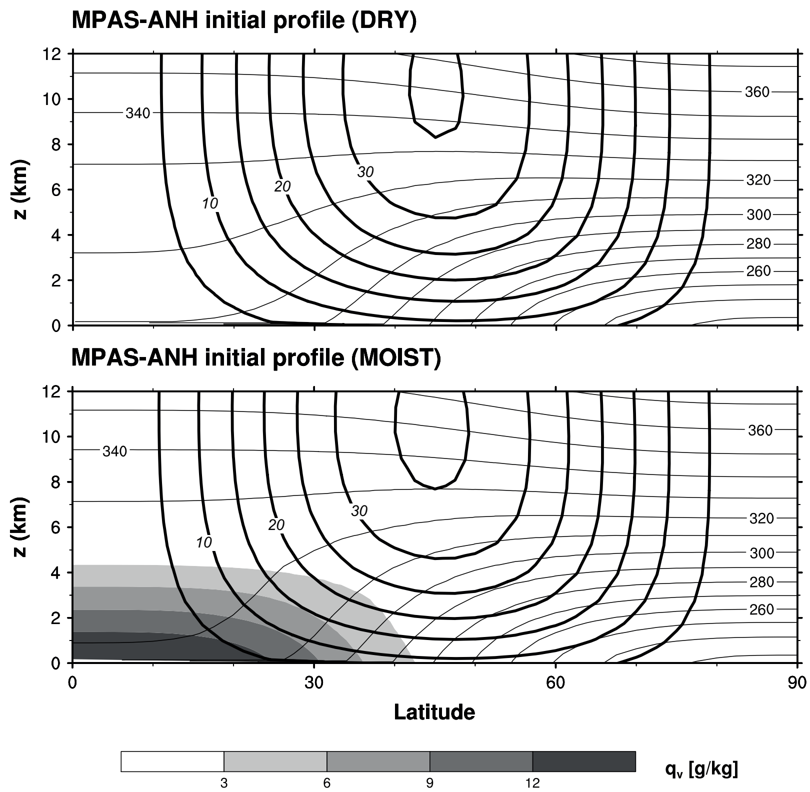

FIG. 2. The dry (top) and moist (bottom) jets from the nonhydrostatic MPAS initialization. Plotted as in Figure 1 with u_{max} is 35.3 m/s in the dry and $u_{max} = 35.7$ m/s and $q_{v\,\mathrm{max}} =$ 15.07 g/kg in the moist case.

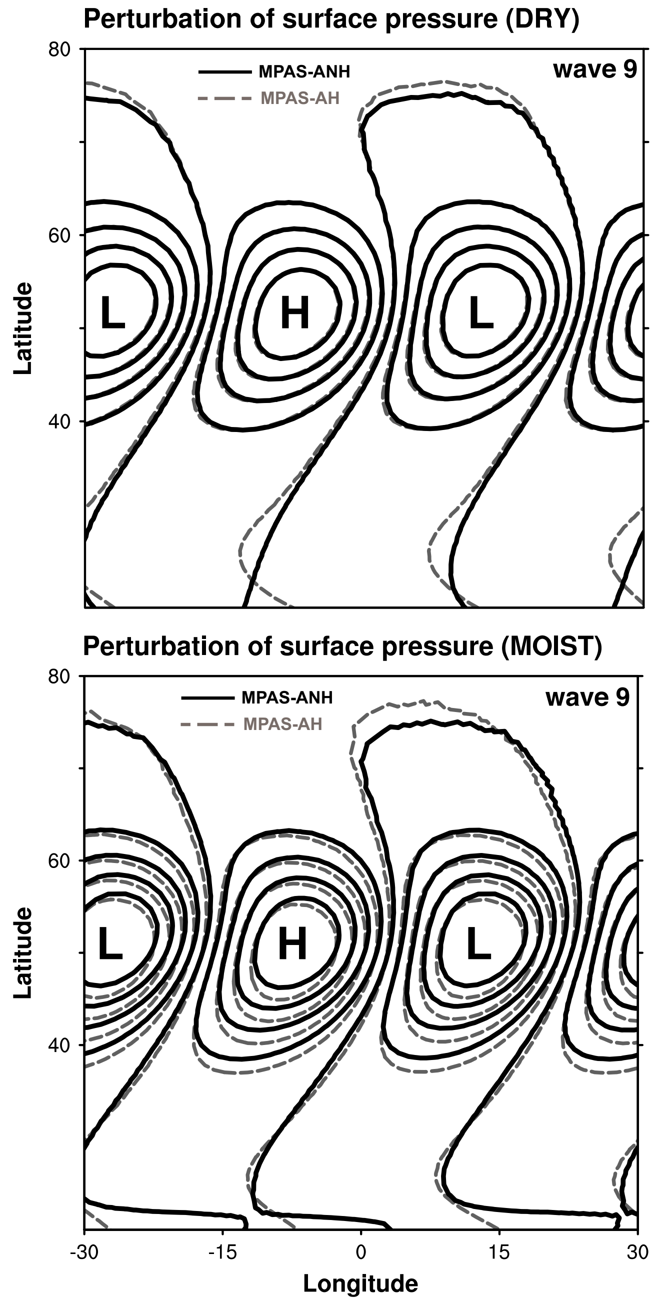

FIG. 3. A part of wave number 9's linearly converged solution for perturbation of surface pressure for MPAS-AH (gray dotted line) and MPAS-ANH (black solid line). The character "L" and "H" denote the surface cyclone and anti-cyclone, respectively. The contour interval is 2 hPa.

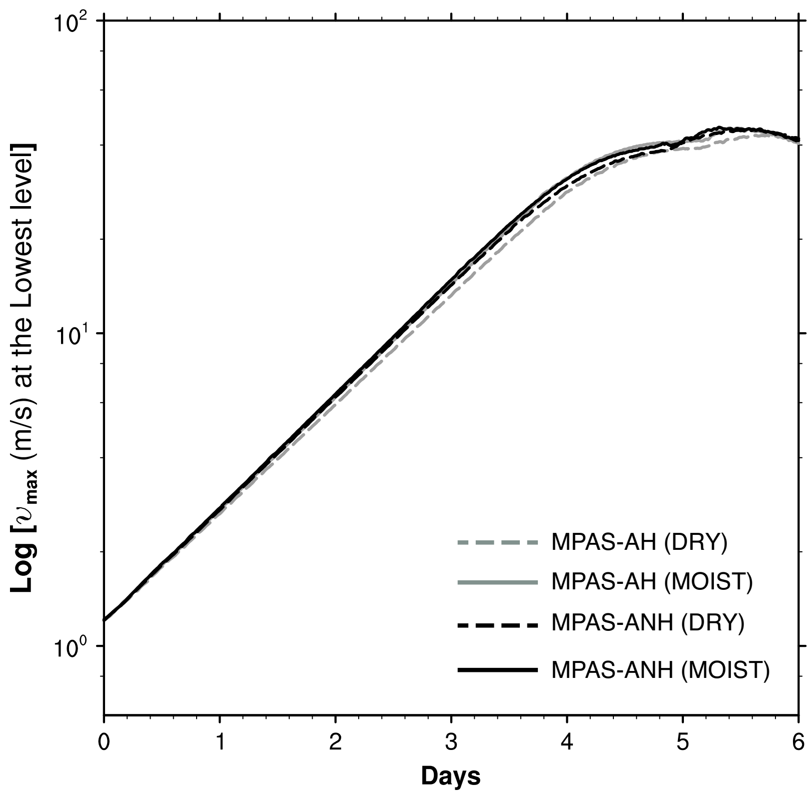

FIG. 4. Maximum meridional wind at the lowest model level during the nonlinear evolution. Nonhydrostatic and hydrostatic results are shown using black and gray line, respectively (dashed lines are used for the dry cases and solid lines for the moist cases).

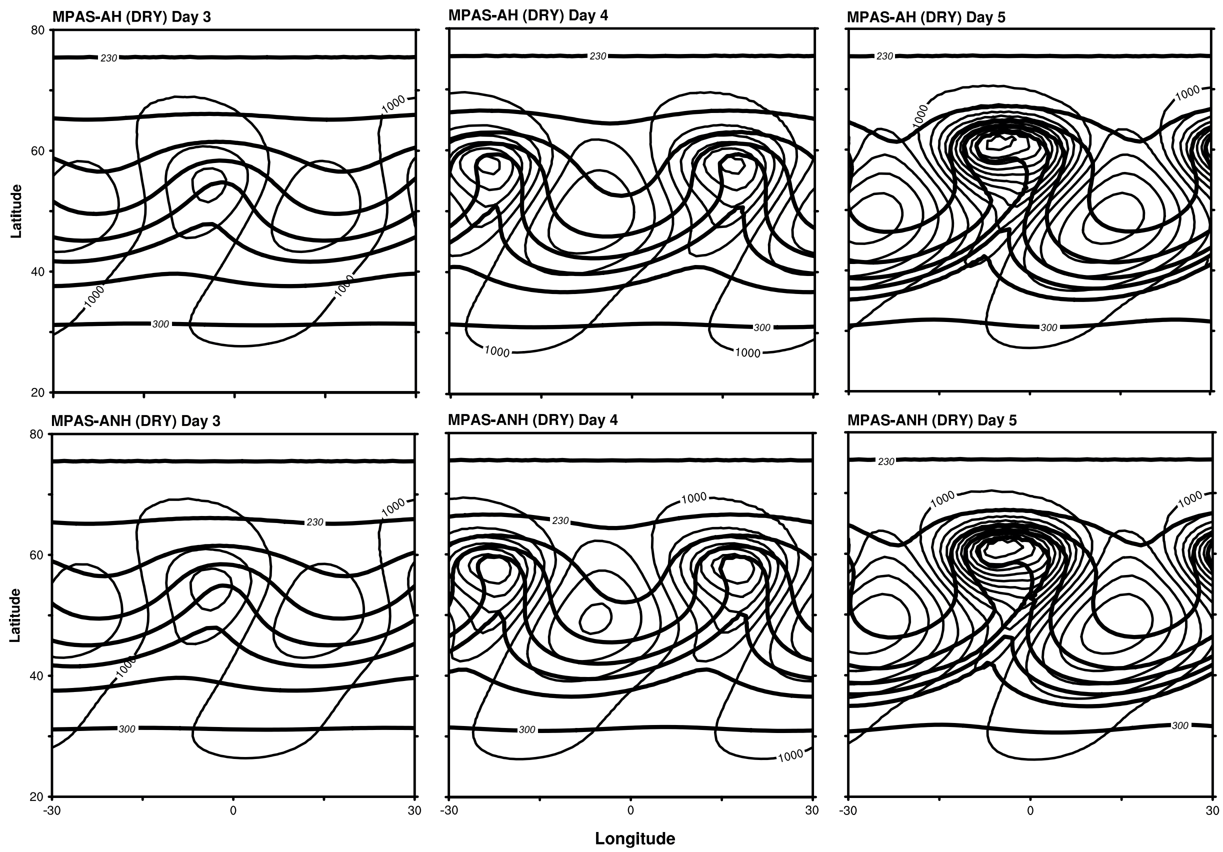

FIG. 5. MPAS-AH (upper) and MPAS-ANH (lower panel) solutions for dry test case. Contours are plotted for θ at the lowest level (thick solid, contour interval is 10 K) and surface pressure (thin solid, contour interval is 4 hPa). Minimum and maximum surface pressures are shown in Table 3.

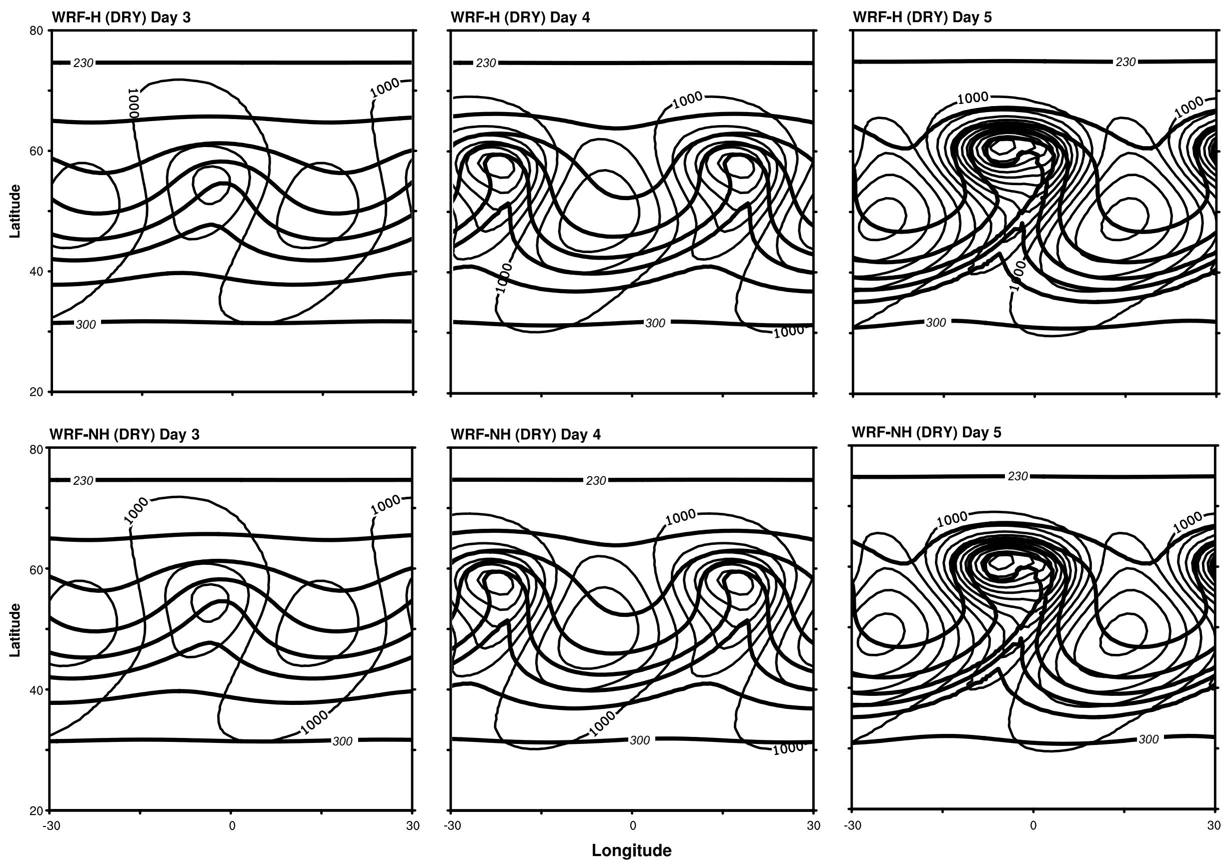

Fig. 6. Hydrostatic WRF (upper) and nonhydrostatic WRF (lower) solutions for the dry test case. Plotted as in Figure 6.

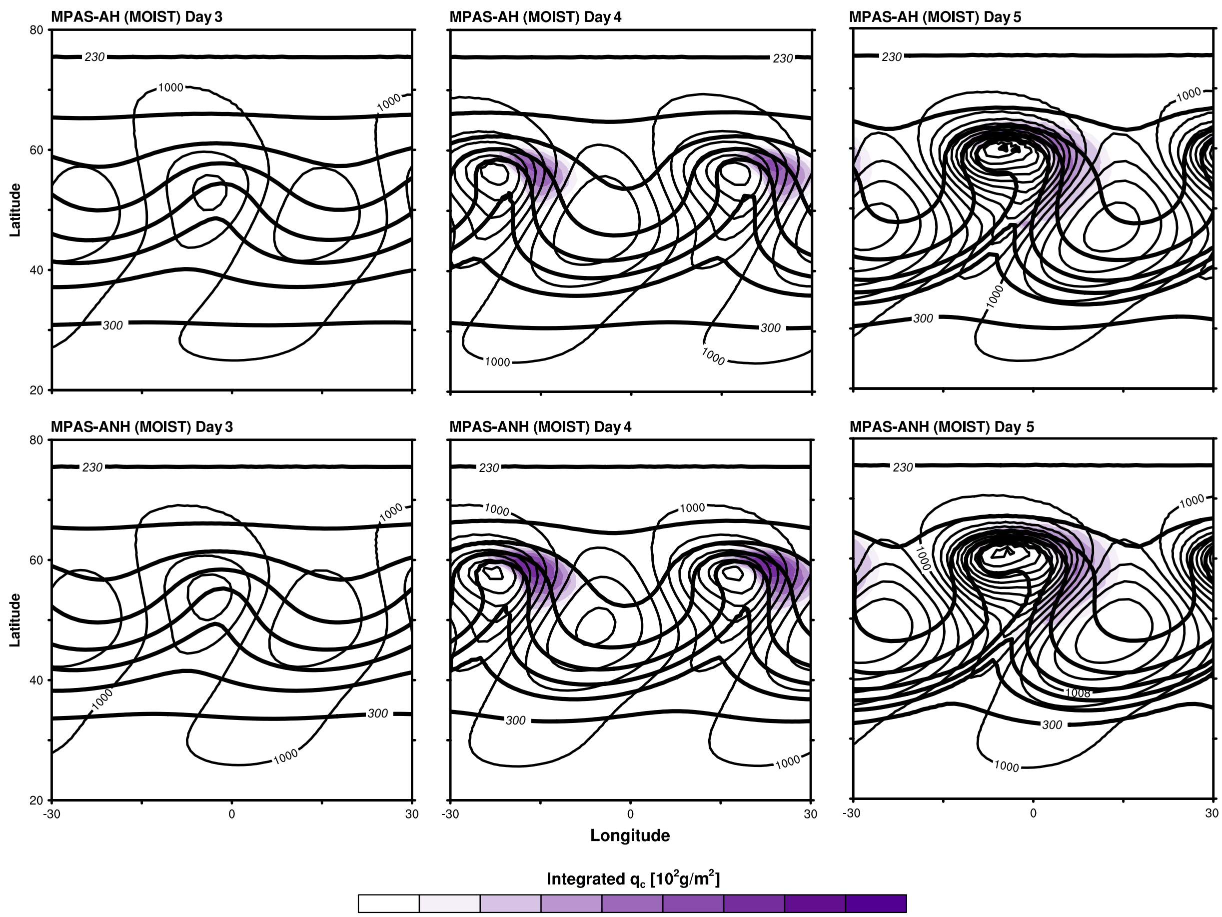

FIG. 7. Moist test case results, plotted as in Figure 6 with the addition of vertically integrated cloud water (q_c, color shading).

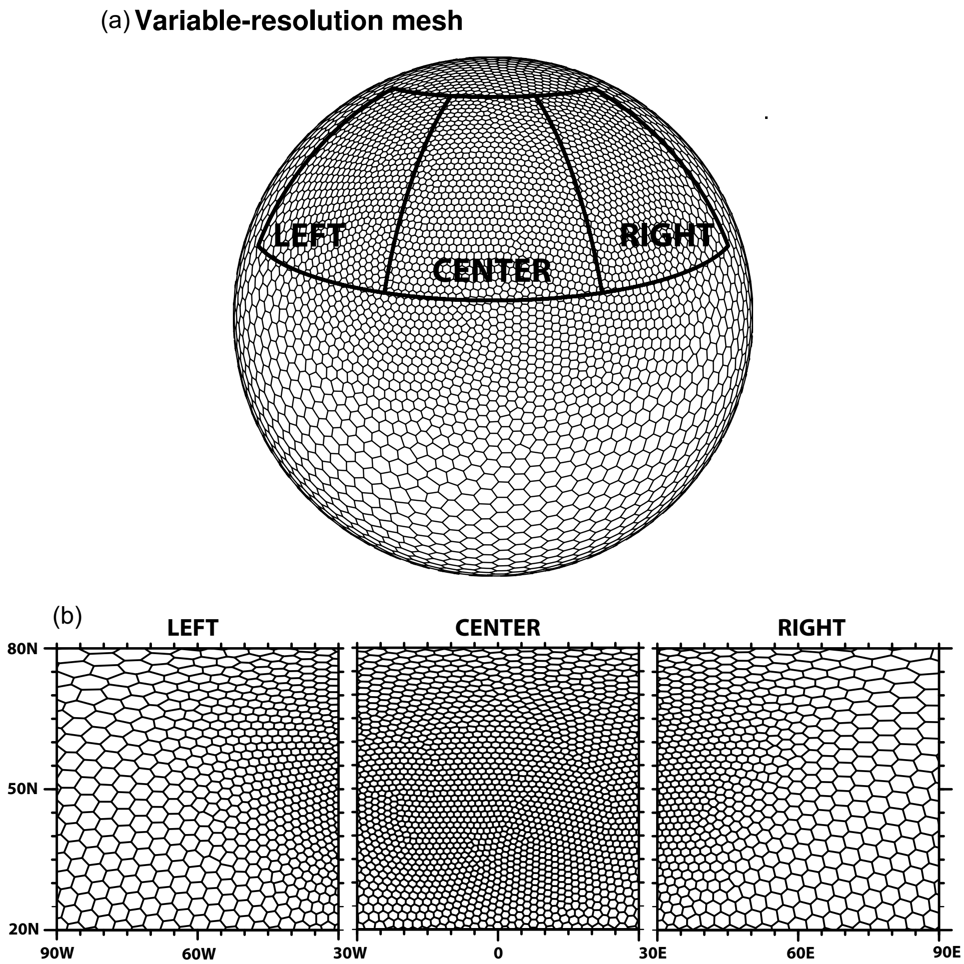

FIG. 8. (a) Mesh structure for variable-resolution grid and analysis subdomain for 5762 cell (coarser than experimental grid for display purposes). LEFT area has its domain on 20°N ∼ 80°N, 90°W ∼ 30°W, CENTER area on 20°N ∼ 80°N, 30°W ∼ 30°E and RIGHT area on 20°N ∼ 80°N, 30°E ∼ 90°E. (b) Each domain's detailed mesh structure from (a).

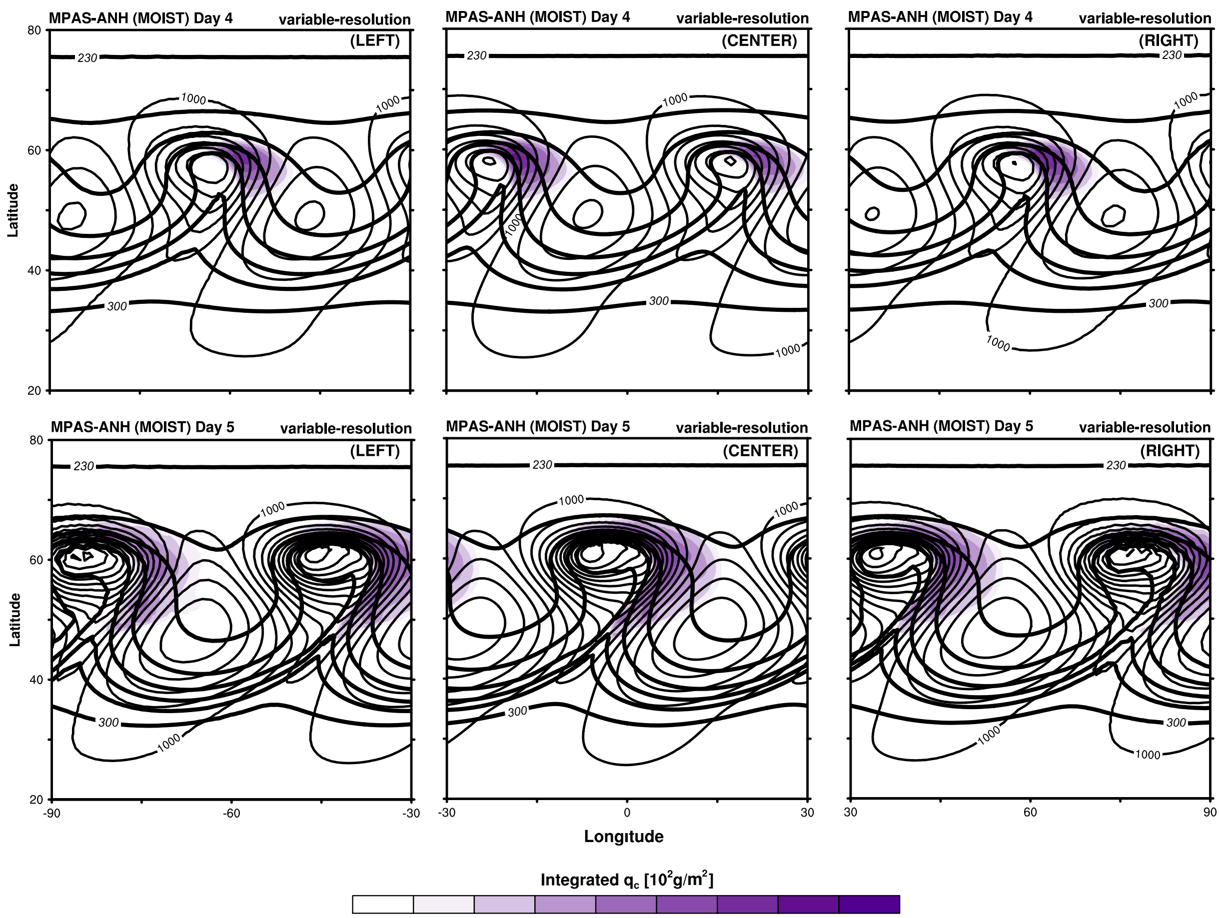

FIG. 9. Plotted variable resolution's results in MPAS-ANH as in Figure 8 (upper and lower panels are day 4 and day 5 results, respectivel). From left to right panel, results are shown based on location which is indicated in Fig. 9. Maximum and minimum surface pressures for each area are shown in Table 5.

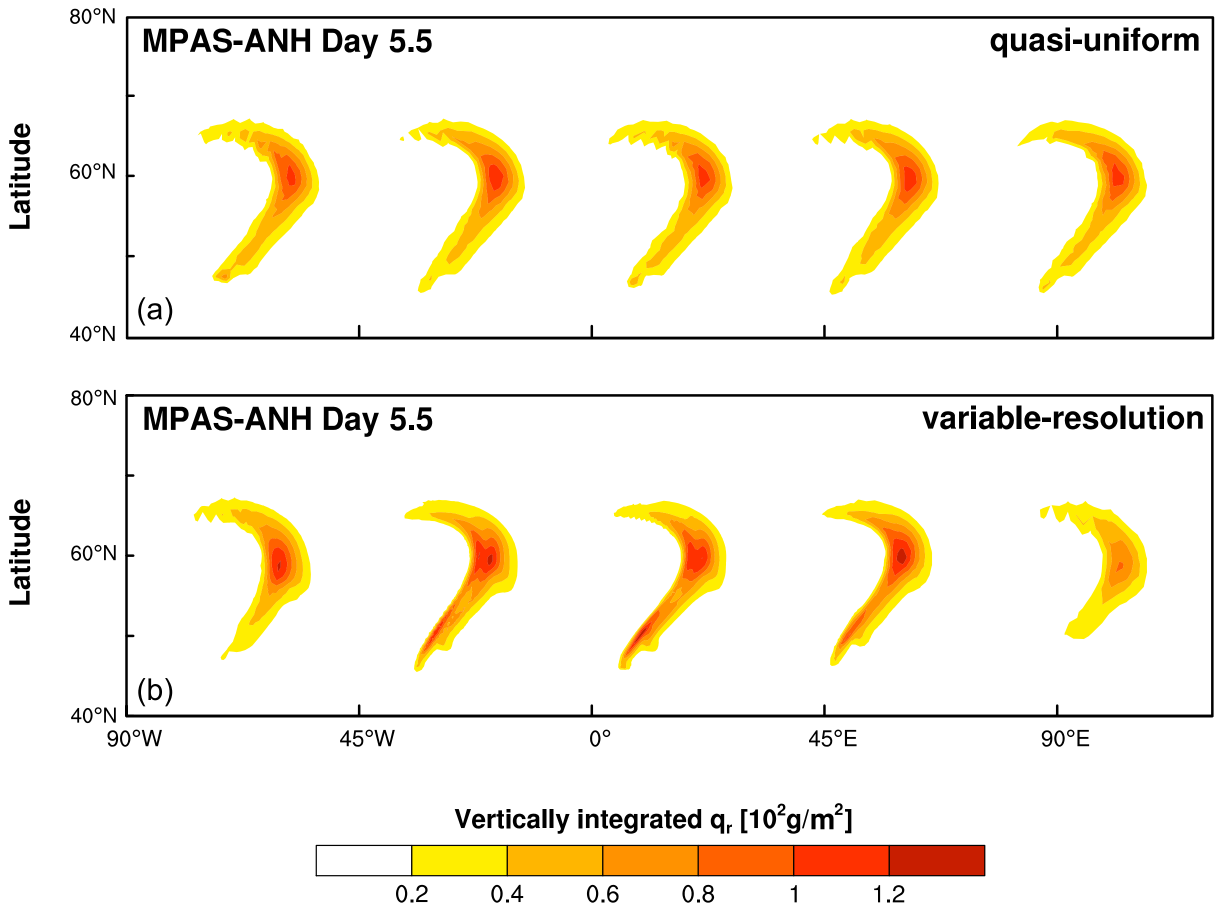

FIG. 10. (a) Vertically integrated cloud rain (q_r) from quasi-uniform and (b) variable resolution in MPAS-ANH.